


Article

Modulating Micro-Arc Oxidation Coating Properties on 6061 Aluminum Alloy via OH⁻ to F⁻ Ion Ratio Optimization

Bing Li ^{1,†}, Heping Lei ^{1,2,†}, Xing Yang ^{1,*}, Xiuxiang Liao ^{1,*}, Zhu Huang ^{1,3}, Daichao Hao ⁴ and Bingchun Jiang ^{1,*} 

¹ School of Mechanical and Electrical Engineering, Guangdong University of Science and Technology, Dongguan 523083, China

² School of Materials Science and Engineering, Hunan University of Science and Technology, Xiangtan 411201, China

³ School of Mechanical and Electrical Engineering, Jiangxi University of Science and Technology, Ganzhou 341000, China

⁴ Dongguan Readore Technology Co., Ltd., Dongguan 523083, China; harrison.hao@readore.com

* Correspondence: yangxing_2024@163.com (X.Y.); xiuxiang_liao@foxmail.com (X.L.); jiangbingchun_2008@163.com (B.J.); Tel.: +86-15728134593 (B.J.)

† These authors contributed equally to this work.

Abstract: We investigate the influence of the NaOH to KF ratio in a silicate electrolyte on the corrosion resistance and tribological properties of micro-arc oxidation (MAO) coatings on a 6061 aluminum alloy. By optimizing the electrolyte composition, we achieved significant improvements in coating quality. The surface morphology and composition of the coatings were characterized using scanning electron microscopy (SEM), energy dispersive spectroscopy (EDS), and X-ray diffraction (XRD). Our findings reveal that the coatings produced at a 2:1 NaOH/KF ratio exhibited superior corrosion resistance, with a corrosion potential of -1.279 V, corrosion current density of 1.85×10^{-7} A·cm⁻², and protective resistance of 1.50×10^5 Ω·cm². Additionally, the surface roughness and coating thickness were measured at 0.68 μm and 8.04 μm, respectively, providing a robust foundation for enhancing the anticorrosive and wear-resistant properties of 6061 aluminum alloy.

Keywords: micro-arc oxidation; 6061 aluminum alloy; corrosion resistance; tribological properties; electrolyte optimization



Academic Editor: Saideep Muskeri

Received: 5 January 2025

Revised: 20 January 2025

Accepted: 27 January 2025

Published: 1 February 2025

Citation: Li, B.; Lei, H.; Yang, X.; Liao, X.; Huang, Z.; Hao, D.; Jiang, B. Modulating Micro-Arc Oxidation Coating Properties on 6061 Aluminum Alloy via OH⁻ to F⁻ Ion Ratio Optimization. *Coatings* **2025**, *15*, 157. <https://doi.org/10.3390/coatings15020157>

Copyright: © 2025 by the authors. Licensee MDPI, Basel, Switzerland. This article is an open access article distributed under the terms and conditions of the Creative Commons Attribution (CC BY) license (<https://creativecommons.org/licenses/by/4.0/>).

1. Introduction

The 6061 aluminum alloy, a key member of the 6XXX series of wrought aluminum alloys, is extensively employed in aerospace, automotive, and machinery manufacturing due to its exceptional combination of properties. These include a low density (~ 2.7 g/cm³), high specific strength (tensile strength of 124–290 MPa), and excellent corrosion resistance, making it ideal for lightweight structural applications. Additionally, its good plasticity, weldability, and machinability allow for versatile processing through casting, forging, and extrusion while maintaining dimensional stability under mechanical loads. These attributes make 6061 aluminum alloy a preferred material for components requiring high strength-to-weight ratios and durability in demanding environments. Despite these advantages, its inherent limitations in hardness and corrosion and wear resistance restrict its use in high-performance engineering applications. Enhancing these properties is, therefore, of substantial practical importance for broadening the application scope of this alloy [1,2].

Surface treatment technologies represent a viable strategy for improving the surface characteristics of aluminum alloys. These include electroplating and chemical plating [3,4],

organic and inorganic coatings [5,6], surface spraying [7], anodic oxidation [8], and micro-arc oxidation (MAO) [9]. MAO technology, in particular, has gained prominence for its ability to in situ grow ceramic-like oxide coatings on metal surfaces, thereby significantly enhancing surface hardness and corrosion resistance. The technology is favored for its ease of operation, simplicity of process, and environmental benefits, holding considerable promise for upgrading the wear and corrosion resistance of aluminum alloy surfaces.

Several studies have highlighted the sensitivity of the MAO coating's structure and performance to various factors, including applied power mode, voltage and current, frequency, duty cycle, oxidation time, and electrolyte composition and concentration [9–13]. Among these, electrolyte components stand out as a primary factor influencing the coating's organization, morphology, and performance, playing a crucial role in the deposition of coating-forming substances onto the substrate surface.

NaOH is a prevalent pH adjuster in electrolyte solutions, the addition of NaOH not only favors the continuous growth of coatings but also helps to increase the thickness of the coatings. However, excessively high NaOH concentrations can lead to strong discharge, compromising the densification of the outer layer. Qin et al. [14] demonstrated that, while the rate of coating formation increases with NaOH concentration, an overabundance of NaOH can result in a looser outer layer and reduced densification. The addition of fluorides, such as NaF, KF, and K_2TiF_6 [15–17], to the electrolyte solution also significantly influences coating quality, wear resistance, and corrosion resistance. For instance, Dong et al. [15] found that incorporating KF into a silicate-based electrolyte enhanced coating growth rates but also increased surface porosity. Wang et al. [18] reported that coatings prepared with 8 g/L sodium fluoride exhibited good corrosion resistance and consistent performance. However, in many studies, alkaline phosphate and silicate electrolytes and some additives such as KF, sodium hydroxide, and potassium hydroxide were used to obtain coatings. However, most of the scholars studied the effect of one of the components of hydroxide and fluoride on the micro-arc oxidized coatings, and few studies have been conducted on the ratio of the hydroxide to fluoride concentration in the electrolyte [19–21].

This study aims to optimize the NaOH/KF ratio in the electrolyte to achieve complete, uniform, and continuous coatings with smooth and flat surfaces. Additionally, it investigates the influence of different NaOH/KF ratios on the corrosion resistance and tribological properties of the coatings, providing a theoretical basis for selecting optimal electrolyte ratios in micro-arc oxidation processes. The primary objective is to explore the effect of the OH^- to F^- ion ratio on the properties of micro-arc oxidation coatings on 6061 aluminum alloy, with the goal of enhancing coating performance in terms of corrosion resistance and mechanical properties.

2. Experiment

2.1. Material Preparation

Experiments were conducted using extruded 6061 aluminum alloy as the substrate, with the following main component mass fractions: Mg (0.8%–1.2%), Si (0.4%–0.8%), Fe (0.7%), Cu (0.15%–0.4%), Mn (0.15%), Cr (0.25%), Zn (0.25%), Ti (0.15%), and the remainder Al. Specimens measuring 20 mm × 15 mm × 3 mm were precision-cut using wire EDM technology. A ϕ 3 mm through-hole thread was machined at the top of each specimen for secure fixation.

Prior to experimentation, the specimens were meticulously sanded with 400 #, 800 #, and 1200 # sandpaper to achieve a smooth and level surface. During the setup, the anode was affixed to the specimen with aluminum screws, while the cathode was attached to a U-shaped stainless steel plate. The micro-arc oxidation (MAO) process was performed using a 30 A MAO power supply in constant voltage mode, with a termination voltage of

480 V, a frequency of 800 Hz, a duty cycle of 30%, and an oxidation duration of 15 min. A water chiller cooling system was employed to maintain the electrolyte temperature at a stable 20 ± 2 °C.

The reagents used in the experiment, including sodium silicate nonahydrate ($\text{Na}_2\text{SiO}_3 \cdot 9\text{H}_2\text{O}$), sodium hydroxide (NaOH), potassium fluoride dihydrate ($\text{KF} \cdot 2\text{H}_2\text{O}$), sodium dihydrogen phosphate (NaH_2PO_4), and glycerol ($\text{C}_3\text{H}_8\text{O}_3$), were all of AR grade and purchased from Shantou Xilong Science Co., Ltd., Shantou, China. To investigate the impact of NaOH/KF ratios on the MAO coating performance, five experimental groups were established with ratios set at 0:1, 1:0, 1:1, 1:2, and 2:1, respectively. These experimental protocols were designated as A₀₁, A₁₀, A₁₁, A₁₂, and A₂₁ (refer to Table 1 for detailed parameters).

Table 1. Electrolyte formulation under different scenarios.

Scheme	Na_2SiO_3 (g/L)	NaH_2PO_4 (g/L)	$\text{C}_3\text{H}_8\text{O}_3$ (g/L)	NaOH(g/L)	$\text{KF} \cdot 2\text{H}_2\text{O}$ (g/L)	NaOH/KF
A ₀₁	12	12	3	0	2	0:1
A ₁₀	12	12	3	2	0	1:0
A ₁₁	12	12	3	2	2	1:1
A ₁₂	12	12	3	2	4	1:2
A ₂₁	12	12	3	4	2	2:1

2.2. Characterization and Performance Testing of Coatings

The performance of the microarc oxidation (MAO) coatings on aluminum alloy substrates was evaluated using a multifaceted approach involving both electrochemical and physical characterization techniques.

Electrochemical characterization included dynamic potential polarization curves and electrochemical impedance spectroscopy (EIS) measurements, which were conducted using a CHI604E electrochemical workstation. A typical three-electrode system was employed, with the specimen serving as the working electrode, a saturated calomel electrode as the reference, and a platinum electrode as the auxiliary electrode. For EIS testing, the coatings were immersed in a 3.5% NaCl solution for 30 min before performing the measurement with an initial potential of the open-circuit potential. The frequency range was set from 10^{-2} Hz to 10^5 Hz, with an amplitude of 0.01 V. Kinetic potential polarization curves were obtained post-immersion in the same corrosion solution, with a scanning potential range from -2 V to 0 V and a scanning rate of 0.5 mV/s. The Zview 2 software was utilized for EIS data fitting, while Tafel extrapolation was applied to determine the corrosion potential (E_{corr}) and corrosion current density (I_{corr}).

The coating thickness was measured using a Minitest 2500-thickness gauge (ElektroPhysik, Cologne, Germany), with 20 random points recorded to calculate the average value. The cleaned specimens were embedded in epoxy resin, sequentially ground with 400# and 2000# sandpaper, and polished. After drying, the specimens were gold-sputtered, and the surface and cross-sectional morphologies of the coatings were examined using a Phenom XL G2 scanning electron microscope (SEM, Funa Scientific Instruments (Shanghai), Co., Ltd., Shanghai, China). Elemental analysis was performed using energy-dispersive spectroscopy (EDS). Surface porosity, pore size, and pore number were quantified using the Image-J software (version 1.54m).

The electrolyte pH was measured with a PHS-3C pH meter, and conductivity was assessed using a DDS-307A conductivity meter (Changzhou Zhongjie Experimental Instrument Co., Ltd., Changzhou, China). The microhardness of the coatings was evaluated with an HVS-1000Z Vickershardness tester (Beijing Times Guangnan Testing Technology Co., Ltd, Beijing, China), with 15 random measurements under a test force of 4.9 N and a loading time of 10 s, to determine the average hardness.

Tribological properties were investigated using an HT-1000 ball-disk high-temperature friction and wear tester (Lanzhou Zhongke Kaihua Technology Development Co., Lanzhou, China). The wear test involved an AISI 52100 steel ball ($\phi 6$ mm, Luoyang Zhisheng Special Steel Ball Co., Ltd., Luoyang, China) as the friction partner, with a load of 2 N, a rotary table speed of 200 r/min, a rotating radius of 5 mm, and a wear duration of 30 min.

3. Results and Discussion

3.1. Effects of Different Electrolyte Ratios on Current, Conductivity and pH Value

Figure 1 delineates the relationship between voltage, current, and oxidation time for 6061 aluminum alloy under varying electrolyte ratios. The data reveal that, under constant voltage mode, the current for each specimen increases and subsequently decreases as oxidation time elapses. This behavior is attributed to the sharp voltage increase during the anodic oxidation stage, where the growing blocking effect of the passivation coating on the current—continuously generated on the aluminum substrate surface—results in a peak between 120 and 140 s before stabilization. The stabilization is further influenced by factors such as electrolyte composition and concentration, voltage settings, electrolyte temperature, the distance between the workpiece and the electrode, and the sealing conditions of the electrolytic tank. Notably, the peak currents for the A₁₂ and A₂₁ schemes are higher and comparably close, with the A₂₁ scheme experiencing a more pronounced decline post-peak, whereas the A₁₂ scheme exhibited a milder decrease. In contrast, the A₁₀ scheme exhibited the lowest peak current with minimal fluctuation, a trend related to the electrolyte's conductivity.

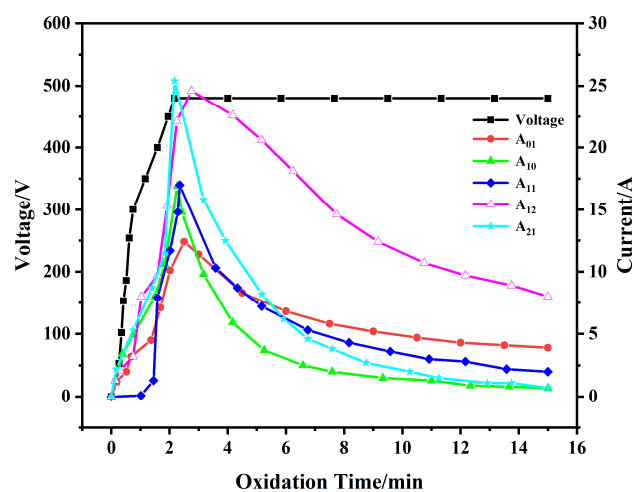


Figure 1. Voltage–time and current–time curves with different schemes.

Figure 2 illustrates the changes in electrolyte conductivity and pH across different experimental schemes. The analysis indicates that, in schemes A₀₁, A₁₁, and A₂₁, where KF concentration remains constant, both electrolyte conductivity and pH values rise with increasing NaOH concentration due to the fact that NaOH can ionize Na⁺ and OH[−] completely in the water. Conversely, in schemes A₁₀, A₁₁, and A₁₂, where NaOH concentration is held fixed, KF concentration increases did not markedly influence the electrolyte's pH, yet conductivity rose with higher KF levels, which was attributed to the fact that KF could ionize K⁺ and F[−], but the hydrolysis of F[−] in water was weak, so the effect on pH was not significant. This suggests that both NaOH and KF concentrations play a role in modulating electrolyte conductivity and pH, with NaOH's influence being more pronounced.

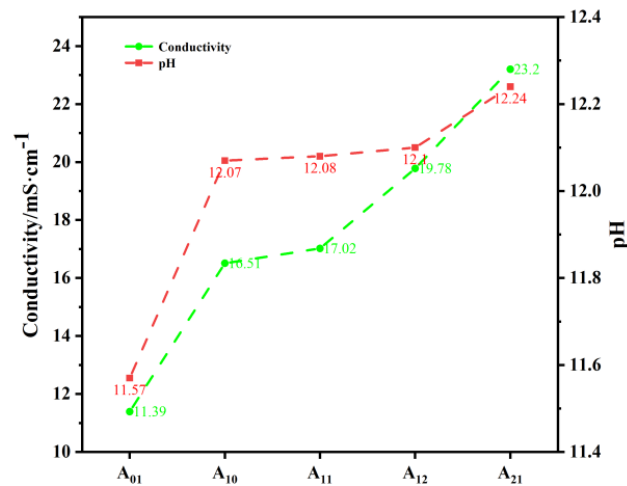


Figure 2. Conductivity and pH value of different electrolytes.

The A₂₁ scheme's electrolyte demonstrated the highest conductivity, while the A₀₁ scheme, lacking NaOH, exhibited the lowest. Correlating this with the peak current data from Figure 1, it is evident that electrolyte conductivity significantly impacts current changes during the micro-arc oxidation process. An increase in conductivity typically correlates with an elevated peak current, highlighting the importance of electrolyte composition in the MAO process.

3.2. Macroscopic Morphology of Micro-Arc Oxidized Layer

Figure 3 presents the macroscopic morphology of the 6061 aluminum alloy surface post-micro-arc oxidation treatment across various process schemes. The findings indicate that, under schemes A₁₀, A₁₁, and A₂₁, the aluminum alloy surfaces were successfully coated with complete, uniform, continuous, and smooth micro-arc oxidation coatings. Conversely, the surfaces under schemes A₀₁ and A₁₂ exhibited noticeable white bumps and a rough texture, significantly degrading the surface quality, which could be attributed to the insufficient OH⁻ and the unstable formation of passivation film leading to the decrease of densification and increase of porosity, which, in turn, affected the quality and appearance of the film layer.

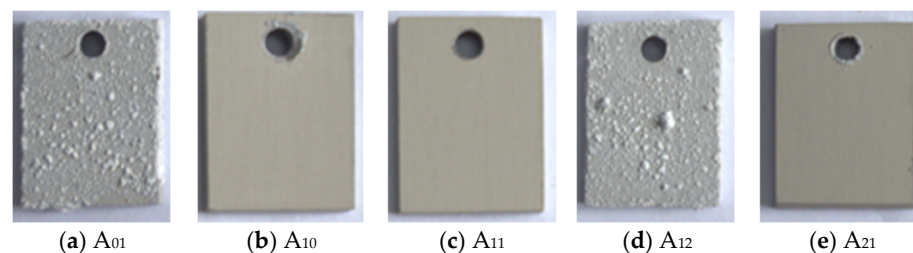


Figure 3. Macro-morphologies of MAO coatings with different schemes.

The electrolyte's NaOH/KF ratio was found to profoundly influence the coating's apparent quality. Notably, when the KF concentration surpassed that of NaOH, the formation of a high-quality coating on the sample surface was challenging. Given these observations, further performance characterization was focused solely on the specimens treated with the A₁₀, A₁₁, and A₂₁ schemes, as they demonstrated the most promising coating quality.

3.3. Micro-Morphology of the Micro-Arc Oxidized Coatings

Figure 4 depicts the surface and cross-sectional micro-morphology of specimens A₁₀, A₁₁, and A₂₁ following micro-arc oxidation treatment. All samples exhibit a characteristic

“crater” morphology, a result of the micro-arc oxidation process where the arc repeatedly penetrates the oxide coatings, leading to gas discharge and the formation of microporous structures. The molten oxide is then ejected through these micropores, coming into contact with the electrolyte solution and rapidly solidifying, which contributes to the coating’s accumulation and rough texture.

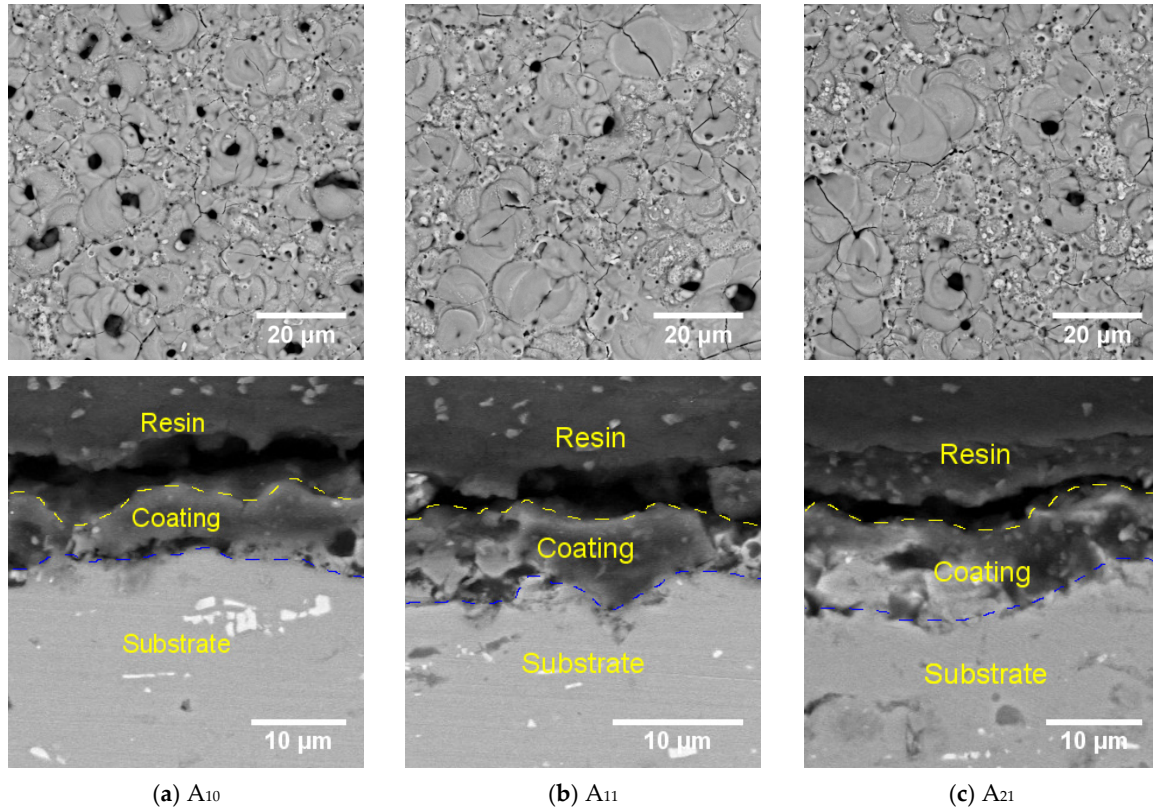


Figure 4. Surface micro-morphologies of micro-arc oxidation coatings.

Visible cracks on the coating surface are attributed to the rapid temperature rise in localized areas during micro-arc oxidation, causing the melting of oxides on the aluminum alloy surface. The differential thermal expansion coefficients between the aluminum alloy matrix and the oxide coatings generate thermal stresses that are not evenly distributed. When these thermal stresses exceed the coating’s tensile strength, cracks, and microcracks form [22,23].

Comparing A₁₀ with A₁₁, we observe that the A coating, which includes KF, has a reduced microporous aperture size. The number of large-diameter micropores decreases, yet the coating’s thickness increases. This reduction in surface micropore size is related to the breakdown phenomenon during the later stages of the micro-arc oxidation process. The addition of KF to the electrolyte increases the amount of molten material deposited within the coatings, which covers the surface micropores and reduces the number of large pores.

The microporous aperture at the “crater” surface of A₂₁ is significantly reduced, primarily due to the higher concentration of NaOH in the electrolyte, which enhances the electrolyte’s conductivity as shown in Figure 2. This increased conductivity leads to a more intense spark discharge during the micro-arc oxidation process, forming additional discharge channels. Since the operating voltage remains constant, the discharge energy does not increase substantially, resulting in a decrease in the gas produced per discharge channel. Consequently, the pore size of the microporous holes is reduced.

Table 2 presents the statistical data on the number and porosity of different pore sizes on the surface of the coatings under various schemes. The analysis of this data reveals that the A₁₀ specimen had a surface porosity of 6.26%, with 26 micropores larger than 2 μm . In contrast, the A₁₁ specimen exhibited a lower surface porosity of 5.44%, a reduction of approximately 13% compared to A₁₀. This was accompanied by a decrease in large pores by 15 and a significant increase in medium (1–2 μm) and small (0–1 μm) pores by 46 and 488, respectively. When comparing A₁₁ with A₂₁, the latter showed a surface porosity of 4.29%, a 21% reduction compared to A₁₁, with decreases in large, medium, and small pores by 1, 26, and 420, respectively. These findings suggest that the addition of KF and an increase in the NaOH concentration both effectively reduce the surface porosity of the coatings.

Table 2. The number of different pore sizes and porosity on the surface of the coatings under different schemes.

Samples	Small Pore (0~1 μm)	Medium Pore (1~2 μm)	Big Pore (>2 μm)	Porosity/%
A ₁₀	1108	40	26	6.26
A ₁₁	1596	86	11	5.44
A ₂₁	1176	60	10	4.29

Figure 5 illustrates the thickness and surface roughness of the micro-arc oxidized coatings under different process conditions. The data show that the surface roughness and coating thickness follow the order: A₂₁ > A₁₁ > A₁₀. Correlating this with Table 2, it can be inferred that the addition of KF enhances the discharge effect during micro-arc oxidation, leading to a higher number of discharge sparks and a faster growth rate of the coatings. This results in more discharge channels and an increase in the number of micropores and the thickness of the coatings. Increasing the NaOH concentration promotes the production of coating-forming substances, further enhancing the growth rate of the coatings. The presence of more coating-forming substances at the discharge channel mouths contributes to the increased thickness of the coatings. Additionally, some substances with lower melting points may flow back into the discharge channel, which could account for the reduced porosity observed.

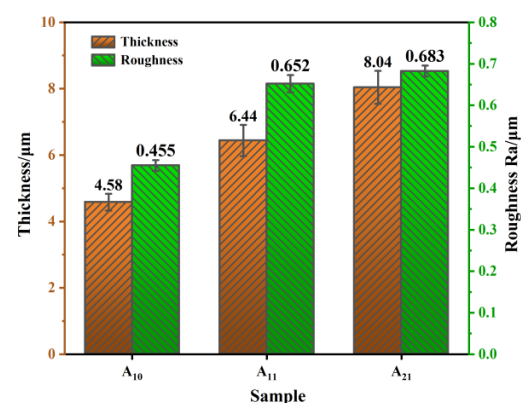


Figure 5. Thickness and surface roughness of micro-arc oxidized coatings for different schemes.

Table 2 and Figure 5 indicate that the addition of KF and the increase in the NaOH concentration in the electrolyte both play a role in reducing surface porosity and increasing coating thickness, which is beneficial for enhancing the wear and corrosion resistance of the coatings.

3.4. Elemental Distribution and Phase Composition of Coatings

3.4.1. Elemental Composition

Figure 6 presents the results of energy dispersive spectroscopy (EDS) for the surface elements of the A₁₀, A₁₁, and A₂₁ coatings. The analysis reveals that the A₁₀ coating is primarily composed of Al, Si, O, P, and other elements. In contrast, after the addition of KF in the A₁₁ and A₂₁ schemes, the coatings contain Al, Si, O, F, and P elements. The Al element is derived from the aluminum alloy matrix, while O, F, and P are introduced from the electrolyte. Si is primarily sourced from the electrolyte, with a minor contribution from the matrix.

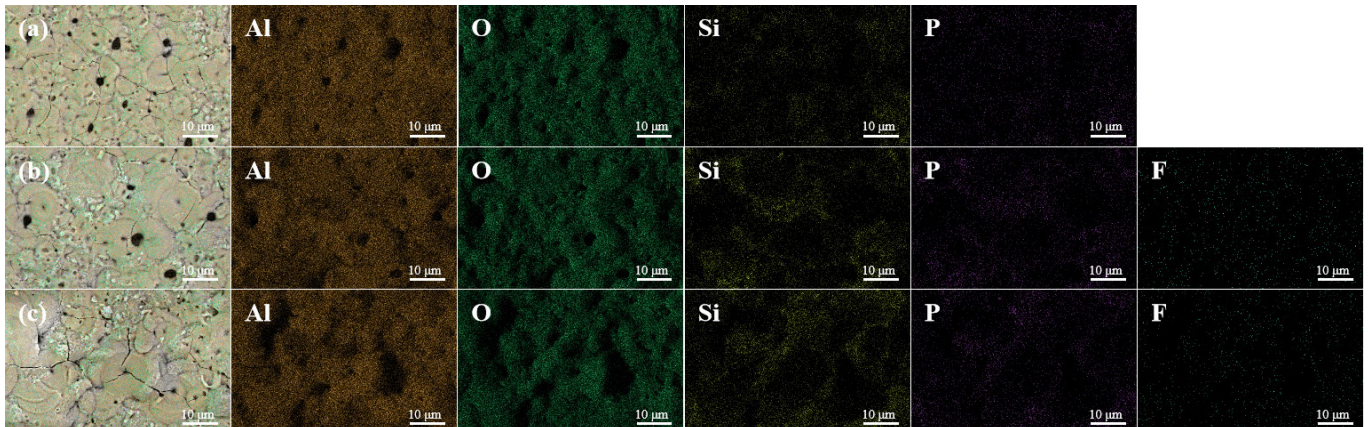


Figure 6. Elemental distribution on the surface of MAO coatings (a) A₁₀; (b) A₁₁; (c) A₂₁.

Figure 7 displays the surface scanning spectra of the coating regions. It is evident that the addition of KF leads to a reduction in Al content in the A₁₁ coatings, with a concurrent increase in Si and P content, and a slight increase in O content. In the A₂₁ coatings, where the NaOH concentration is increased, the Al content is reduced, and there is a significant increase in the O and Si content, while the P and F contents remain largely unchanged. These elemental distribution patterns suggest that KF addition facilitates the incorporation of P, Si, and O from the electrolyte into the coatings, whereas the NaOH concentration increase primarily affects the incorporation of Si and O elements.

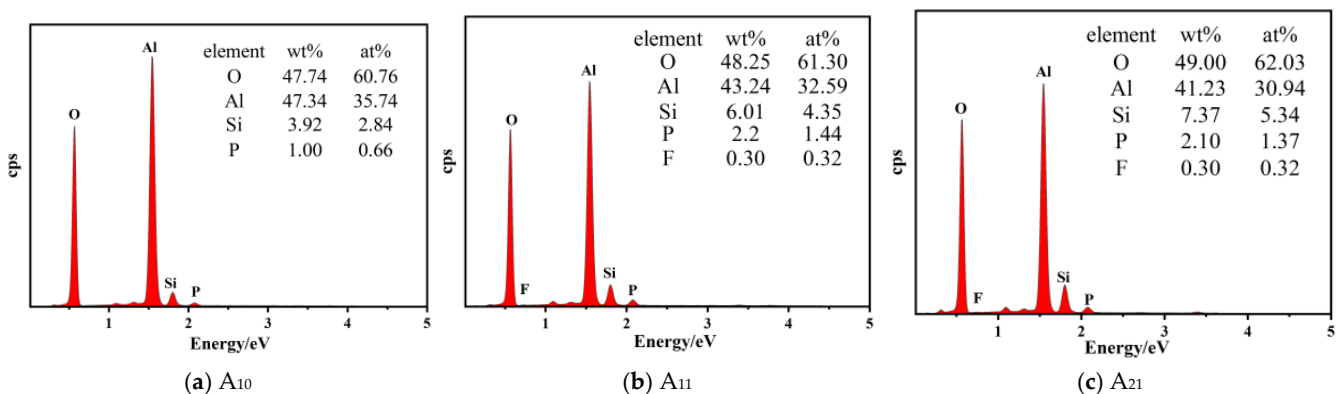


Figure 7. Scanning spectra of different schemes of micro-arc oxidized coating level.

3.4.2. Physical Phase Analysis

To delve deeper into the physical phase constitution of the coatings, XRD analysis was conducted. Figure 8 illustrates the XRD spectra for the A₁₀, A₁₁, and A₂₁ coatings. The spectral data reveal that these layers are predominantly composed of Al, α -Al₂O₃, γ -Al₂O₃, mullite, AlF₃, and additional phases. The Al phase is derived from the coating matrix. The

emergence of the other phases is likely attributed to ionic interactions occurring within the electrolyte. Hypothetical formation reactions for these phases might include the following:

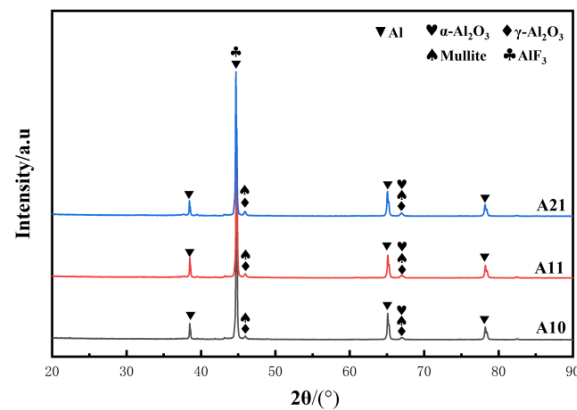
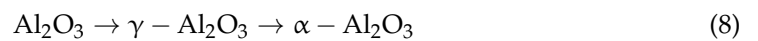
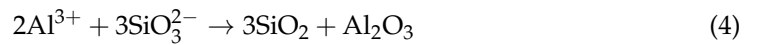


Figure 8. XRD patterns of MAO coatings with different processes.

These observations suggest that the physical phase composition of the coatings is profoundly influenced by the types and concentrations of cations and anions present in the electrolyte. The presence of α - Al_2O_3 and mullite phases in the A₁₁ and A₂₁ coatings is likely the result of reactions between the Si and F-elemental components of Al_2O_3 within the electrolyte. The formation of the AlF_3 phase can be attributed to the F^- ions present in the electrolyte, which underscores the pivotal role of electrolyte composition in determining the physical phase composition of the coatings. These findings further confirm that the choice and concentration of electrolyte components can significantly alter the coating's properties, highlighting the importance of electrolyte selection in the micro-arc oxidation process.

NaOH plays a dual role in the alumina formation reaction by supplying the necessary O^{2-} ions and regulating the solution's pH and conductivity. Concurrently, the presence of F^- ions enhances the spark density during the reaction, increasing the number of discharge channels within the coatings. This facilitates the entry of more anions into the layer to participate in the reaction, thereby providing a wealth of coating-forming substances.

The XRD spectra in Figure 8 reveal the presence of both α - Al_2O_3 and γ - Al_2O_3 phases in all coatings. When a high voltage is applied to the material surface, molten alumina is ejected through the discharge channels and rapidly cools upon contact with the electrolyte, leading to the formation of the γ - Al_2O_3 phase. During this process, numerous fine bubbles are generated on the microporous surface of the discharge channels. As indicated in reference [24], the unstable γ - Al_2O_3 phase tends to transform into the stable α - Al_2O_3 phase over time. The formation of α - Al_2O_3 not only densifies the ceramic coating but also

enhances its hardness and corrosion resistance, as noted in reference [25]. Moreover, the reaction environment promotes the formation of mullite.

The peak intensities in the XRD spectra of A₁₀, A₁₁, and A₂₁ do not show significant changes, suggesting that variations in the KF and NaOH concentrations in the electrolyte do not markedly affect the content of the physical phases within the coatings. This is further supported by the elemental analysis results shown in Figure 7.

3.5. Corrosion Resistance of Coatings in Neutral NaCl Media

3.5.1. Kinetic Potential Polarization Curves

Figure 9 presents the kinetic potential polarization curves for the substrate and the coatings of various schemes, with the fitting results detailed in Table 3. The analysis reveals that the corrosion current density (J_{corr}) follows the order $A_{21} > A_{10} > A_{11}$, from smallest to largest. The corrosion potential of the micro-arc oxidation-treated specimens shifted positively compared to the substrate, suggesting a reduced corrosion tendency for each coating.

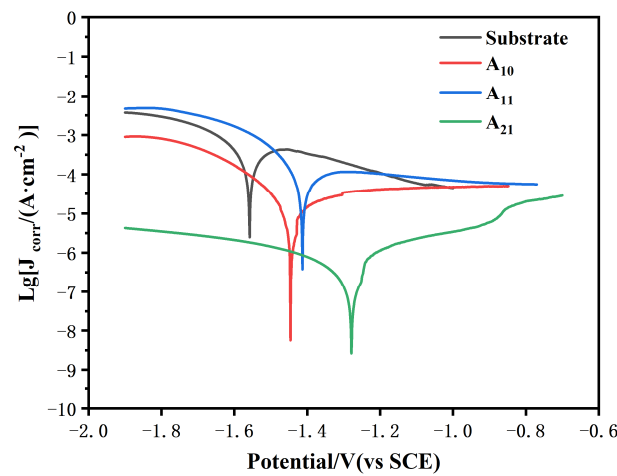


Figure 9. Dynamic potential polarization curves of substrate and MAO coatings with different processes.

Table 3. Fitting results of dynamic potential polarization curves.

Samples	E_{corr}/V	$J_{\text{corr}}/(A \cdot \text{cm}^{-2})$	$R_p/(\Omega \cdot \text{cm}^2)$
Substrate	−1.558	6.68×10^{-4}	118
A ₁₀	−1.446	1.32×10^{-6}	3.28×10^3
A ₁₁	−1.413	1.30×10^{-4}	406
A ₂₁	−1.279	1.85×10^{-7}	1.50×10^5

Specifically, the J_{corr} for the A₁₀ and A₁₁ schemes decreased by from 0 to 2 orders of magnitude, while the A₂₁ scheme experienced a reduction of 3 orders of magnitude relative to the substrate. Additionally, the polarization resistance (R_p) for the three schemes increased by from 0 to 3 orders of magnitude, indicating a significant enhancement in corrosion resistance after micro-arc oxidation treatment. This change in current density indicates a semi-passivation effect, i.e., corrosion products fill the pores and cracks within the protective layer, which is similar to a previously reported study [26,27].

The A₁₀ scheme, which lacked KF in the electrolyte, exhibited a small J_{corr} . Despite the thinness of the A₁₀ coatings and the presence of microcracks, the layer's dense composition effectively blocked NaCl medium penetration, thereby enhancing electrochemical corrosion resistance. In contrast, the A₁₁ scheme, with KF addition, showed a slight increase in J_{corr} . Although the coating thickness of the A₁₁ scheme increased, the higher surface porosity and increased number of micropores (as detailed in Table 2) provided more pathways for corrosive media infiltration, leading to a reduction in corrosion resistance.

The A_{21} scheme, with an increased NaOH concentration, demonstrated the lowest J_{CORR} and the highest E_{CORR} , which can be attributed to its lowest porosity and the fewer micropores and macropores. This suggests that the coating with A_{21} possesses the highest corrosion resistance in a neutral NaCl medium among the tested schemes.

3.5.2. Electrochemical Impedance Spectra

Figure 10 depicts the electrochemical impedance spectra of the 6061 aluminum alloy substrate and the coatings produced under the A_{10} , A_{11} , and A_{21} schemes. Figure 11 illustrates the equivalent circuit model used to analyze the coatings, where R_s denotes the solution resistance, R_1 and CPE_1 represent the resistance and capacitance of the external sparse layer, respectively, and R_2 and CPE_2 represent the resistance and capacitance of the internal dense layer, respectively. The fitting results for this model are provided in Table 4.

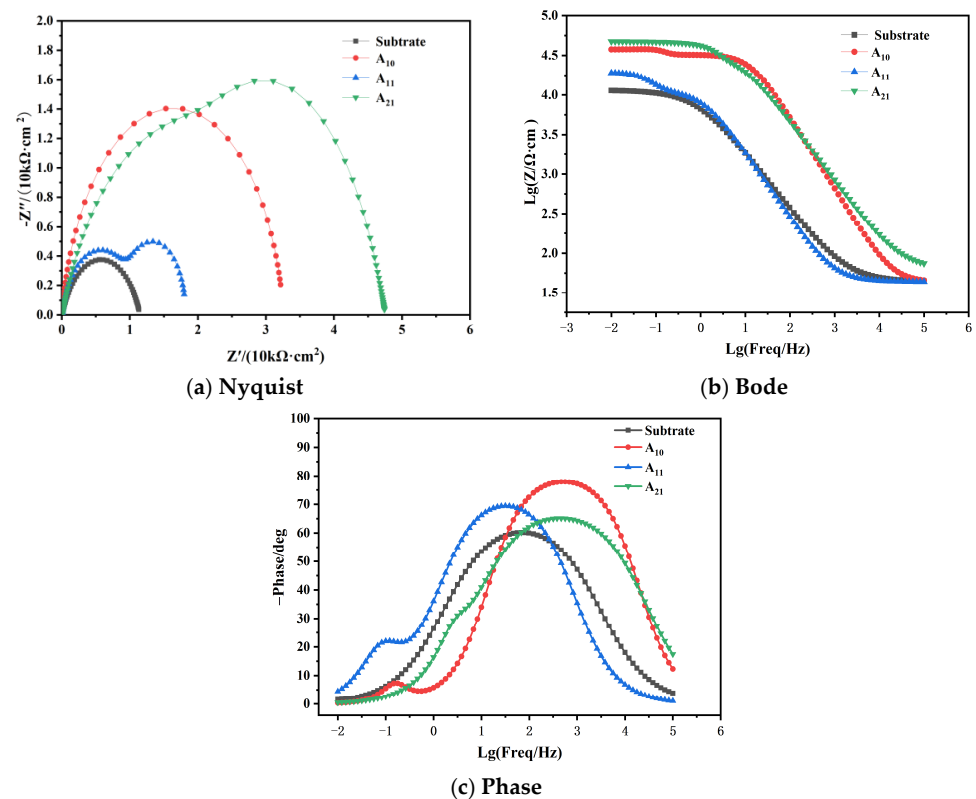


Figure 10. EIS spectra of the micro-arc oxidized coatings for the substrate and different schemes: (a) Nyquist plot, (b) Bode plot and (c) Phase plot.

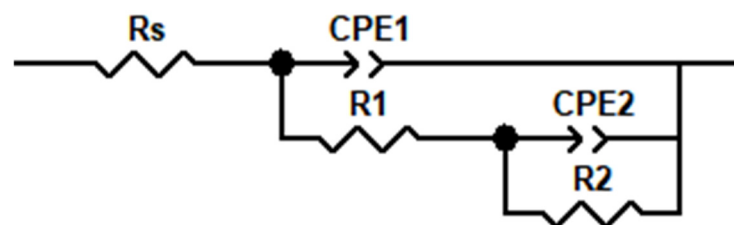


Figure 11. Equivalent circuit of coatings.

The Nyquist plots in Figure 10 show that the impedance modulus and the capacitive arc radius for the coatings of schemes A_{10} , A_{11} , and A_{21} are greater than those of the substrate. This suggests that the micro-arc oxidized specimens offer improved resistance to the penetration of the NaCl corrosive medium compared to the substrate, thereby significantly enhancing the corrosion resistance in neutral NaCl solution.

Table 4. EIS fitting results for different schemes of coatings.

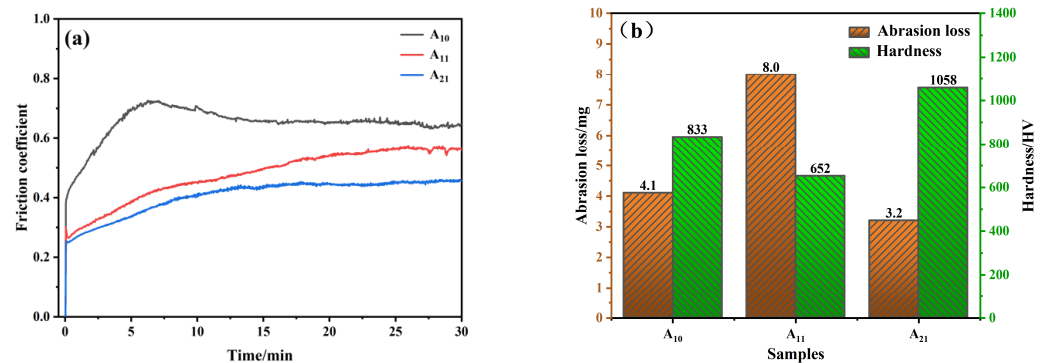
Serial Number	$R_s^\alpha/\Omega \cdot \text{cm}^2$	CPE ₁		$R_1^\alpha/\Omega \cdot \text{cm}^2$	CPE ₂		$R_2^\alpha/\Omega \cdot \text{cm}^2$
		$\Upsilon_0^b/\Omega^{-1} \text{cm}^{-2} \text{S}^n$	n^e		$\Upsilon_0^b/\Omega^{-1} \text{cm}^{-2} \text{S}^n$	n^e	
A ₁₀	44.51	4.69×10^{-7}	0.92	22,166	6.31×10^{-7}	0.83	10,371
A ₁₁	37.21	1.85×10^{-5}	0.85	10,043	2.57×10^{-4}	1.06	6314
A ₂₁	62.19	1.52×10^{-6}	0.76	37,370	5.38×10^{-6}	0.94	12,973

The fitting results in Table 4 reveal that the R_2 values for the coatings of schemes A₁₀, A₁₁, and A₂₁ are lower than the R_1 values. This indicates that the external sparse layer of the coatings plays a pivotal role in determining its corrosion resistance. The relatively lower resistance of the internal dense layer may be attributed to structural defects within this layer, which facilitate the penetration of the corrosive medium and, consequently, reduce the overall corrosion resistance of the coatings.

3.6. Friction and Wear Properties of Coatings

The abrasion resistance of the micro-arc oxidized coatings is influenced by several factors, including the coefficient of friction, surface hardness, coating thickness, and porosity [28,29]. The reduction of the friction coefficient and the increase in surface hardness are crucial for enhancing the wear resistance of the coatings [30,31].

Figure 12 presents the friction coefficient, abrasion loss, and hardness of the coatings under different schemes. Figure 12a indicates that the friction coefficient of the coatings follows the order A₂₁ > A₁₁ > A₁₀, from highest to lowest. Figure 12b shows that the abrasion loss of the coatings is A₁₁ > A₁₀ > A₂₁, while the hardness of the coatings is A₂₁ > A₁₁ > A₁₀, both in descending order.

**Figure 12.** (a,b) Friction coefficient, abrasion loss, and hardness of coatings of different schemes.

The A₁₁ coating has a lower coefficient of friction compared to A₁₀, which may be attributed to its higher number of small pores on the surface and lower surface hardness. These factors result in reduced frictional resistance during rubbing with the friction vice. The lower coefficient of friction for A₂₁ compared to A₁₁ is primarily due to its higher hardness and lower porosity, which reduce the wear area in contact with the friction partner. Consequently, the abrasion loss of A₂₁ is less than that of A₁₁, possibly because of the denser structure of the A₂₁ coating, which is more effective at resisting wear.

Among the three schemes, the A₂₁ coating exhibits the best wear resistance, followed by A₁₁ and then A₁₀, highlighting the importance of both hardness and porosity in determining the wear properties of the coatings.

Figure 13 provides insights into the wear morphology of the coatings under different programs. The analysis of the figure reveals several key points regarding the wear resistance of the coatings:

1. The A_{10} coating exhibits the largest wear track profile, with a mix of smooth areas and wear areas, indicating a significant wear effect by the friction vice. Despite the large wear track profile, the abrasion loss for A_{10} is lower than that of A_{11} due to its higher porosity, which allows for some wear areas to be discontinuous.
2. The A_{11} coating, which includes KF, shows the most intense abrasion, with a high number of smooth areas on the surface. The friction vice's wear effect on this layer is substantial, potentially due to the accumulation of debris in the coating's depressions, increasing the contact area and thus the wear area.
3. In contrast, the A_{21} coating has the smallest wear track profile, with the surface primarily characterized by wear zones. The wear amount for A_{21} is reduced by 60% compared to A_{11} . While the porosity of A_{21} and A_{11} is similar, the higher surface hardness of A_{21} and the smaller wear area contribute to its lower abrasion loss.

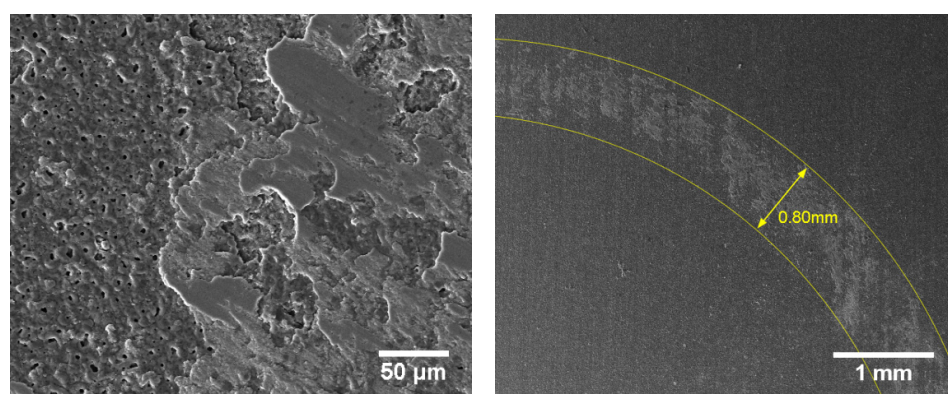
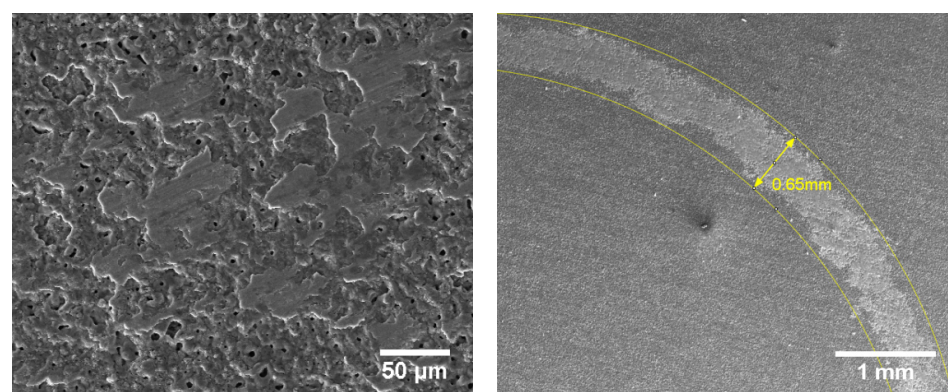
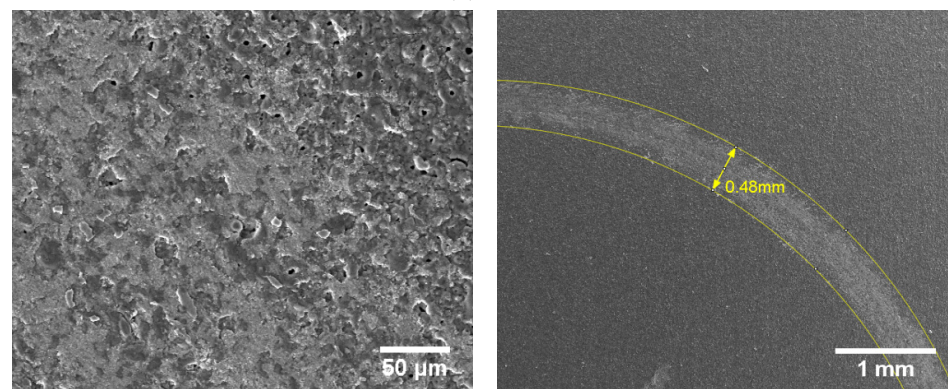
(a) A_{10} (b) A_{11} (c) A_{21}

Figure 13. Wear patterns of coatings under different schemes.

The comprehensive analysis of the friction and coefficient of friction curves, abrasion loss, surface wear morphology, and hardness suggests that the coatings under the A₂₁ scheme possess the best wear resistance, followed by A₁₁. The A₁₀ scheme exhibits the worst wear resistance, likely due to its lower surface hardness and higher porosity, which make it more susceptible to wear.

4. Conclusions

- (1) In the silicate electrolyte used for micro-arc oxidation on the surface of 6061 aluminum alloy, NaOH and KF are crucial components for coating formation. NaOH aids in the development of a passivation coating on the substrate's surface and enhances the solution's conductivity, while KF intensifies the discharge effect, leading to a higher growth rate of the coatings and an increased rate of coating-forming material deposition. Meanwhile, the data show that adding KF and increasing the NaOH concentration can effectively reduce the size of micropores and decrease the porosity of the coating surface and that adding KF will significantly increase the number of micropores.
- (2) The formation of a high-quality micro-arc oxidized coating is dependent on the NaOH/KF ratio in the electrolyte. A ratio of 0:1 or 1:2 prevents the formation of a coating with good quality. However, ratios of 1:0, 1:1, and 2:1 result in coatings that are complete, uniformly continuous, and smooth, suggesting that the KF content should not exceed NaOH to achieve a high-quality coating. The abrasion resistance of the micro-arc oxidized coatings is affected by the addition of KF. The A₁₁ exhibits decreased abrasion resistance compared to the A₁₀. Increasing the NaOH concentration can mitigate the negative impact of KF on the coating's abrasion resistance. The A₂₁ demonstrates the best overall performance in terms of abrasion resistance, hardness, and wear amount.
- (3) The corrosion resistance of the micro-arc oxidized coatings in a neutral NaCl solution is markedly improved compared to the 6061 aluminum alloy substrate. A₂₁ shows the highest corrosion resistance among the tested schemes. Electrochemical impedance spectra analysis reveals that the micro-arc oxidized coatings possess a higher impedance modulus and capacitive arc radius than the substrate, signifying a superior resistance to the penetration of the NaCl corrosive medium. The fitting results indicate that the external sparse layer of the coatings is a key factor in determining its corrosion resistance.

In summary, the optimal conditions for the micro-arc oxidation process 6061 aluminum alloy involve a balanced NaOH/KF ratio, which not only affects the coating formation process but also the resulting coating's mechanical and corrosion properties. The A₂₁ solution, with a NaOH/KF ratio of 2:1, emerges as the most effective in producing a coating with excellent wear and corrosion resistance.

Author Contributions: Conceptualization, D.H.; methodology, B.L. and X.Y.; investigation, H.L. and X.L.; data curation, H.L., X.L. and Z.H.; writing—original draft, B.L., H.L., X.Y. and X.L.; writing—review and editing, B.L. and B.J.; supervision, B.J.; funding acquisition, X.Y. and D.H. All authors have read and agreed to the published version of the manuscript.

Funding: This research was funded by Dongguan Sci-tech Commissioner Program (grant number 20231800500582), Energy Saving and Emission Reduction Innovation Team (GKY-2022CQTD-1) and the Key scientific research projects for general universities of Guangdong province (2023ZDZX3048).

Institutional Review Board Statement: Not applicable.

Informed Consent Statement: Informed consent was obtained from all subjects involved in the study.

Data Availability Statement: Data are contained within the article.

Conflicts of Interest: Daichao Hao is employed by Dongguan Readore Technology Co., Ltd. The remaining authors declare that the research was conducted in the absence of any commercial or financial relationships that could be construed as a potential conflict of interest.

References

1. Wang, Y.C.; Yuan, L.Y.; Yang, L.; Peng, Y.; Ding, W. Strengthening-toughening of high-strength Al-Zn cast aluminum alloys: Research progress and prospects. *Rare Met. Mater. Eng.* **2023**, *52*, 3954–3970.
2. Wang, D.D.; Liu, X.T.; Wu, Y.K.; Han, H.; Yang, Z.; Su, Y.; Zhang, X.; Wu, G.; Shen, D. Evolution process of the plasma electrolytic oxidation (PEO) coating formed on aluminum in an alkaline sodium hexametaphosphate ((NaPO₃)₆) electrolyte. *J. Alloys Compd.* **2019**, *798*, 129–143. [[CrossRef](#)]
3. Gao, J.; Cui, K.; Li, S.; Zhong, L.; Dai, J.; Yang, Z.; Qiang, R. A New Process of Chemical Plating Ni-P Electromagnetic Induction Heating Activation on the Surface of Aluminium Alloy Base Material. *Coatings* **2024**, *14*, 1221. [[CrossRef](#)]
4. Devyatkina, T.I.; Luchneva, S.I.; Vasin, E.N.; Cherkashev, V.V.; Isaev, E.S.; Belyaev; Rogozhin, V.V. Surface preparation of aluminum alloys for electroplating. *Russ. J. Appl. Chem.* **2020**, *93*, 1372–1379. [[CrossRef](#)]
5. Xu, F.; Zhu, S.Z.; Ma, Z. Preparation of inorganic coating by sol-gel method and its thermal protection performance. *Rare Met. Mater. Eng.* **2020**, *49*, 1261–1267.
6. Castro, Y.; Özmen, E.; Durán, A. Integrated self-healing coating system for outstanding corrosion protection of AA2024. *Surf. Coat. Technol.* **2020**, *387*, 125521. [[CrossRef](#)]
7. Wu, Z.; Chen, Y.; Liu, H.; Hua, W.; Duan, J.; Kong, L. A review of the developments of the characteristics and mechanisms of airless spraying on complex surfaces. *Coatings* **2023**, *13*, 2095. [[CrossRef](#)]
8. Baroni, E.; Fortini, A.; Meo, L.; Soffritti, C.; Merlin, M.; Garagnani, G.L. Ball-on-disk wear maps for bearing steel-hard anodized AA6082 aluminum alloy tribocouple in dry sliding conditions. *Coatings* **2024**, *14*, 1469. [[CrossRef](#)]
9. Wang, T.J.; Liu, X.A.; Zhang, K.Y.; Xie, L.; He, M.T.; Lu, Y.L.; Luo, K.Y.; Hu, K.J.; Li, G.Z.; Wang, M.Z. Effect of current density on the wear resistance of ceramic coatings formed on 7075 aluminum alloy via microarc oxidation. *Phys. Met. Metallogr.* **2024**, *prepublish*. [[CrossRef](#)]
10. Wang, D.; Liu, X.; Zhang, Q.; Li, D.L.; Liu, X.; Su, H.; Zhang, Y.; Yu, S.X.; Shen, D. Role of the electrolyte composition in establishing plasma discharges and coating growth process during a micro-arc oxidation. *Surf. Coat. Technol.* **2020**, *402*, 126349. [[CrossRef](#)]
11. Wang, C.; Ma, R.; Du, A.; Fan, Y.; Zhao, X.; Cao, X. Growth methods of PEO coatings on 7075 aluminum alloy at two cathodic current densities. *Surf. Coat. Technol.* **2022**, *432*, 128099. [[CrossRef](#)]
12. Oh, G.H.; Yoon, J.K.; Huh, J.Y.; Doh, J.M. Effect of frequency of plasma electrolytic oxidation on the microstructure and corrosion resistance of 6061 aluminium alloy. *Surf. Coat. Technol.* **2023**, *471*, 129861. [[CrossRef](#)]
13. Yeshmanova, G.; Blawert, C.; Serdechnova, M.; Wieland, D.F.; Starykevich, M.; Gazenbiller, E.; Höche, D.; Smagulov, D.; Zheludkevich, M.L. Effect of electrolyte composition on the formation of PEO coatings on AA2024 aluminium alloy. *Surf. Interfaces* **2024**, *44*, 103797. [[CrossRef](#)]
14. Qin, Y.; Wu, G.H.; Atrens, A.; Zhang, X.L.; Zhang, L.; Ding, W.J. Effect of NaOH concentration on microstructure and corrosion resistance of MAO coating on cast Al–Li alloy. *J. Transactions. Nonferrous. Trans. Nonferrous Met. Soc. China* **2021**, *31*, 913–924. [[CrossRef](#)]
15. Dong, H.R.; Ma, Y.; Wang, S.; An, L.Y.; Yuan, H. Effect of potassium fluoride on growth and microstructure of MAO coatings on AZ91 magnesium alloys. *Rare Met. Mater. Eng.* **2018**, *47*, 249–254.
16. Xie, X.M.; Yang, E.H.; Zhang, Z.Y.; Wei, W.; Li, D.; Zhao, X.; Yang, R.; Li, W. Effects of K₂TiF₆ and electrolyte temperatures on energy consumption and properties of MAO coatings on 6063 aluminum alloy. *Materials* **2023**, *16*, 1830. [[CrossRef](#)] [[PubMed](#)]
17. Sun, S.; Ye, G.; Lu, Z.; Weng, Y.; Ma, G.; Liu, J. Surface treatment of Zn-Mn-Mg alloys by micro-arc oxidation in silicate-based solutions with different NaF concentrations. *Materials* **2021**, *14*, 4289. [[CrossRef](#)]
18. Wang, Y.; Zhang, J.; Wang, W.; Yu, F.; Cao, W.; Hu, S. Effect of sodium fluoride additive on microstructure and corrosion performance of micro-arc oxidation coatings on EK30 magnesium alloy. *Surf. Coat. Technol.* **2024**, *496*, 131628. [[CrossRef](#)]
19. Abbas, A.; Ting-Yi, W.; Hsin-Chih, L. Effects of Electrolyte Compositions and Electrical Parameters on Micro-Arc Oxidation Coatings on 7075 Aluminum Alloy. *J. Compos. Sci.* **2023**, *7*, 472. [[CrossRef](#)]
20. RYU, H.S.; HONG, S.H. Effects of KF, NaOH, and KOH Electrolytes on Properties of Microarc-oxidized Coatings on AZ91D Magnesium Alloy. *J. Electrochem. Soc.* **2009**, *156*, C298–C303. [[CrossRef](#)]
21. Sheng, L.U.; Wang, Z.X.; Chen, J. Optimization of dual electrolyte and characteristic of micro-arc oxidation coating fabricated on ZK60 Mg alloy. *Trans. Nonferrous Met. Soc. China* **2011**, *21*, 929–935.

22. Duan, H.; Du, K.; Yan, C. Electrochemical corrosion behavior of composite coatings of sealed MAO coating on magnesium alloy AZ91D. *Electrochim. Acta* **2006**, *51*, 2898–2908. [[CrossRef](#)]
23. Guo, H.F.; An, M.Z. Growth of ceramic coatings on AZ91D magnesium alloys by micro-arc oxidation in aluminate/fluoride solutions and evaluation of corrosion resistance. *Appl. Surf. Sci.* **2005**, *246*, 229–238. [[CrossRef](#)]
24. Al Bosta, M.M.; Ma, K.J.; Chien, H.H. The effect of MAO processing time on surface properties and low temperature infrared emissivity of ceramic coating on aluminium 6061 alloy. *Infrared Phys. Technol.* **2013**, *60*, 323–334. [[CrossRef](#)]
25. Wang, Y.K.; Sheng, L.; Xiong, R.Z.; Li, B.S. Study of ceramic coatings formed by MAO on Al matrix composite surface. *Surf. Eng.* **1999**, *15*, 112–114. [[CrossRef](#)]
26. Kaseem, M.; Yang, H.W.; Ko, Y.G. Toward a nearly defect-free coating via high-energy plasma sparks. *Sci. Rep.* **2017**, *7*, 2378. [[CrossRef](#)] [[PubMed](#)]
27. Dzhurinskiy, D.V.; Dautov, S.S.; Shornikov, P.G.; Akhatov, I.S. Surface modification of aluminum 6061-O alloy by plasma electrolytic oxidation to improve corrosion resistance properties. *Coatings* **2020**, *11*, 4. [[CrossRef](#)]
28. Borgardt, E.D.; Katsman, A.V.; Krishtal, M.M. Effect of TiN particles on mechanical and anticorrosive properties of oxide layers formed by PEO on silumin. *J. Phys. Conf. Ser.* **2021**, *2144*, 012009. [[CrossRef](#)]
29. Gabor, R.; Prymus, T.; Cvrček, L.; Nehasil, V.; Hlinka, J.; Buřil, M.; Tokarčíková, M.; Seidlerová, J. Final surface modification for better wear resistance of ceramic coating on cast AlSi10Mg alloy. *Ceram. Int.* **2022**, *48*, 37433–37447. [[CrossRef](#)]
30. Li, X.J.; Zhang, M.; Wen, S.; Mao, X.; Huo, W.G.; Guo, Y.Y.; Wang, Y.X. Microstructure and wear resistance of micro-arc oxidation ceramic coatings prepared on 2A50 aluminum alloys. *Surf. Coat. Technol.* **2020**, *394*, 125853. [[CrossRef](#)]
31. Vatan, H.N.; Ebrahimi-Kahrizangi, R.; Kasiri-Asgarani, M. Structural, tribological and electrochemical behavior of SiC nanocomposite oxide coatings fabricated by plasma electrolytic oxidation (PEO) on AZ31 magnesium alloy. *J. Alloys Compd.* **2016**, *683*, 241–255. [[CrossRef](#)]

Disclaimer/Publisher’s Note: The statements, opinions and data contained in all publications are solely those of the individual author(s) and contributor(s) and not of MDPI and/or the editor(s). MDPI and/or the editor(s) disclaim responsibility for any injury to people or property resulting from any ideas, methods, instructions or products referred to in the content.